JOURNAL OF COMPUTATIONAL PHYSICS **123,** 207–225 (1996)
ARTICLE NO. 0017

Multiresolution Schemes for Conservation Laws with Viscosity

BARNA L. BIHARI

Rockwell Science Center, 1049 Camino Dos Rios, Thousand Oaks, California 91360

Received December 19, 1994; revised April 25, 1995
DEDICATED TO THE MEMORY OF AMI HARTEN

This paper presents multiresolution schemes for the efficient numerical solution of one-dimensional conservation laws with viscosity. The method, originally developed by A. Harten (*Commun. Pure Appl. Math.*, to appear) for hyperbolic conservation laws, computes the cell average multiresolution representation of the solution which provides much information about the solution's regularity. As a consequence, the possibly expensive ENO (essentially nonoscillatory) reconstruction as well as numerous flux computations are performed only near discontinuities, and thereby the numerical solution procedure becomes considerably more efficient. The multiresolution scheme is also expected to ''follow'' possibly unsteady irregularities from one time step to the next. When viscosity is added, predicting the location of the irregularity becomes a problem of estimating the change in shock thickness. To this end, we derive shock width estimates for our 1D prototype equations, which, when combined with the stability restriction of the numerical scheme, provide a reliable mechanism for enlarging the original multiresolution stencil. The numerical experiments for scalar conservation laws indicate the feasibility of multiresolution schemes for the viscous case as well. © 1996 Academic Press, Inc.

1. INTRODUCTION

In the process of solving the equations of fluid dynamics numerically, often the grid and therefore the solution are overresolved in large subsets of the computational domain. More precisely, in such regions of smoothness, the fluxes are evaluated too many times, and, if the high-quality but expensive ENO reconstruction is used, it will also be invoked unnecessarily for many grid cells.

Adaptive grid methods can achieve an improvement in efficiency by creating grid points only where large gradients are found. However, the difficulty in programming them for time-dependent problems, as well as the inherent topological constraints in the structured grid case (for two or higher dimensions) are significant disadvantages of adaptive grids. On the other hand, the 1D multiresolution scheme of [7] and its 2D version [2] use equally spaced grids everywhere, even for unsteady problems. Typically, the grid is quite fine, but the method does not compute the fluxes in neighborhoods where the solution is smooth. For many problems this means most of the domain. Since the need for grid clustering is thus eliminated, multiresolution schemes have the potential to also simplify the grid generation process. In 1D the amount of time spent on grid generation is negligible (even for 2D Cartesian grids as shown by [2]); and, as is demonstrated by the short algorithms of [6], the multiresolution modules too are simple. For typical problems, the number of flux computations can thus be reduced by as much as five or six times in both 1D [7, 1] and 2D [2].

In this paper we modify the semi-discrete formulation of the 1D multiresolution scheme [1] to solve the *viscous* model problem. We use the linear wave equation with viscosity (sometimes called the linearized Burgers' equation) and (viscous) Burgers' equation as our prototype linear and nonlinear equations, respectively. Adding viscosity, in general, ''smoothes'' the solution, and in many cases can even stabilize an otherwise unstable numerical scheme. Except for a time step limitation which can be different from its inviscid counterpart, the viscous problem does not pose any complications from the numerical point of view. The multiresolution analysis remains the same as well, since it is concerned only with the regularity of the cell averages of the solution. In the combined scheme, however, the assumption about finite wave speed in the hyperbolic case (and the use of a corresponding CFL number) must be reevaluated. Namely, the ''padding'' for multiresolution purposes of the irregular regions by one cell to the left and to the right may not be adequate for a parabolic equation, where waves can propagte with infinite speed.

Although theoretically disturbances are felt instantly everywhere, their influence diminishes exponentially with distance. By defining an appropriate cutoff point, we can approximate a shock's effective influence to be within a finite distance. In turn, we use this approximate wave speed as a means to enlarge the region of irregularity around the shock so that the necessary cells will be solved for exactly. We use the shock width as a measure of the region where the shock's influence is significant. If we estimate the change in the width from one time step to the next, we can also predict the region where exact computations may be needed. The change in shock width is a function of Δt, which, in turn, must obey the stability limit of the numerical

0021-9991/96 $12.00
Copyright © 1996 by Academic Press, Inc.
All rights of reproduction in any form reserved.

scheme. To complete our analysis, we derive both linear and nonlinear stability conditions for a second-order scheme, which will then lead us to predict the number of cells that the shock can span at the next time step; these cells will be marked for exact flux computations. The subsequent modified scheme will also be tested by performing several numerical experiments, across the mesh Reynolds number range.

The rest of this paper is organized as follows: after setting up the general framework for the numerical scheme in Section 2, in Section 3 we use the closed form exact solution to Burgers' equation to derive a formula for the shock width. In Section 4 linear and nonlinear stability analyses are performed for schemes that are considered "close" to the second-order ENO scheme. We obtain a limit for Δt this way, which in turn will be used in Section 5, in conjunction with the shock width, to estimate the number of cells to be used for enlarging the multiresolution stencil. We conclude with Section 6 by presenting numerical experiments using second-order space and time discretizations and various viscosity coefficients.

2. THE NUMERICAL SCHEME IN 1D

2.1. Finite Volume Discretization

We are solving the initial value problem for the scalar viscous conservation law in one space dimension on $(x, t) \in [-1, 1) \times [0, \infty)$:

$$u_t + f(u)_x = 0, \tag{2.1a}$$

$$u(x, 0) = u_0(x), \tag{2.1b}$$

subject to periodic boundary conditions

$$u(1, t) = u(-1, t), \tag{2.1c}$$

$$u_x(1, t) = u_x(-1, t), \tag{2.1d}$$

where the flux f now includes derivatives of u and we consider its linear and nonlinear versions ($\nu > 0$, $a > 0$):

$$f(u) = au - \nu u_x, \tag{2.2a}$$

or

$$f(u) = \frac{1}{2}u^2 - \nu u_x. \tag{2.2b}$$

Let $\mathbf{E}(t)$ be the time evolution operator, so that

$$u(\cdot, t) = \mathbf{E}(t) \cdot u_0. \tag{2.3}$$

Then the finite volume scheme can be written in the standard conservation form

$$v_j^{n+1} = v_j^n - \lambda(\bar{f}_{j+1/2} - \bar{f}_{j-1/2}) = (\overline{\mathbf{E}}_h(\Delta t) \cdot v^n)_j, \tag{2.4}$$

where $\overline{\mathbf{E}}_h$ is the discrete analog of $\mathbf{E}$, Δt is the time step, and $\bar{f}_{j+1/2}$ is the numerical flux, a function of $2K + 2$ variables:

$$\bar{f}_{j+1/2} = \bar{f}_{j+1/2}(v_{j-K}^n, ..., v_{j+K+1}^n), \tag{2.5}$$

with $2K$ corresponding to the spatial accuracy. As we restrict ourselves to second-order spatial accuracy, K will be assumed to be unity throughout this paper. $\bar{f}$ is either an exact or approximate representation of the flux f given by (2.2). On the other hand, v_j^n is an approximation to the average of the exact solution $u(x, t)$ in the cell $[x_{j-1/2}, x_{j+1/2}]$, $j = 0, ..., N - 1$,

$$v_j^n \approx \frac{1}{\Delta x}\int_{x_{j-1/2}}^{x_{j+1/2}} u(x, t_n)\, dx, \tag{2.6}$$

with $t_n = n\Delta t$ and $\Delta x = 2/N$, N being the number of (uniform) cells in the interval $[-1, 1]$.

We then numerically solve the semi-discrete form of (2.4):

$$(v_j)_t = -\frac{1}{\Delta x}(\bar{f}_{j+1/2} - \bar{f}_{j-1/2}) = S_j \tag{2.7}$$

by using a second-order Runge–Kutta time update, yielding a uniformly second–order scheme.

2.2. Numerical Flux

The numerical flux $\bar{f}$ of (2.5) is a discrete version of (2.2), where the convection and diffusion terms are approximated separately. For the convective part, we reconstruct u from its cell averages using an ENO interpolation, while the u_x derivative is approximated by central differencing. We have, therefore,

$$\bar{f}_{j+1/2}(v_{j-1}, v_j, v_{j+1}, v_{j+2}) = f^{\mathrm{R}}(v_l, v_r) - \nu\frac{v_{j+1} - v_j}{\Delta x}, \tag{2.8}$$

where $f^{\mathrm{R}}(v_l, v_r)$ (here "R" stands for Riemann) is the solution to the Riemann problem given the left and right values of u. Since our prototype equations are scalar, for

f^R we can, without performance penalty, use the exact solution of the Riemann problem, given in [2], among other references. In the linear case, for example, the expression for the convective part simplifies to

$$f^R(v_l, v_r) = av_l. \tag{2.9}$$

Note that the second term in (2.8) corresponds to linearly reconstructing u at the cell interface (using only v_j and v_{j+1}) and then taking its derivative, which, only for the second-order case, coincides with using the cell averages v_j and v_{j+1} to approximate u_x.

2.3. Time Integration

For the time update of (2.7) we use the following second-order Runge–Kutta (RK2) method,

$$\begin{aligned} v_j^{n+1/2} &= v_j^n + \Delta t S_j(v^n), \\ v_j^{n+1} &= \tfrac{1}{2}(v_j^n + v_j^{n+1/2} + \Delta t S^j(v^{n+1/2})). \end{aligned} \tag{2.10}$$

In the above, the symbolic $n + \frac{1}{2}$ index is used to denote an intermediate value of the cell average v_j, computed for the first stage of the RK2 method. The right-hand side S_j is a function of the entire v array, or at least some nontrivial subset thereof (in our notation, dropping the subscripts j from v, means the entire array v). Note that (2.10) is also known as the Heun method.

2.4. Second-Order ENO Reconstruction

To obtain the value of the function u at the cell boundary, we use a piecewise linear reconstruction of u from its cell averages. For the reconstruction an adaptive stencil is used, resulting in a second-order ENO interpolation,

$$v_{j+1/2}^- = v_j + \tfrac{1}{2} M(v_{j+1} - v_j, v_j - v_{j-1}), \tag{2.11a}$$

$$v_{j+1/2}^+ = v_{j+1} - \tfrac{1}{2} M(v_{j+2} - v_{j+1}, v_{j+1} - v_j), \tag{2.11b}$$

with

$$M(a, b) = \begin{cases} a, & \text{if } |a| \le |b|, \\ b, & \text{if } |a| > |b|. \end{cases} \tag{2.11c}$$

The quantities given by (2.11a) and (2.11b) correspond, therefore, to the v_l and v_r used in (2.8), the point values of u to the left and to the right of the cell interface at $j + 1/2$, respectively.

3. SHOCK WIDTH FOR THE NONLINEAR VISCOUS PROBLEM

In this section we focus our attention on Burgers' equation,

$$u_t + uu_x = \nu u_{xx}, \tag{3.1a}$$

with discontinuous initial data,

$$u(x, 0) = \begin{cases} u_0, & \text{if } x < 0, \\ -u_0, & \text{if } x \ge 0, \end{cases} \tag{3.1b}$$

where $u_0 > 0$. We first review the exact solution for this problem, from which we derive the value of u_x at $x = 0$. The shock width δ, which is inversely proportional to $\max_{-\infty<x<\infty} |u_x|$, is then derived as a function of time. It will also be shown, that the change in δ is largest between $t = 0$ and $t = \Delta t$.

3.1. Maximum u_x from the Exact Solution

Via the Cole–Hopf transformation

$$u(x, t) = -2\nu \frac{\phi_x}{\phi}, \tag{3.2}$$

we can derive an exact solution for the general problem (3.1a) (see [3, 11]). In the particular case of initial condition (3.1b), we obtain (from [3])

$$\begin{aligned} &u(x,t) \\ &= -u_0 \frac{2\sinh\dfrac{u_0 x}{2\nu} + e^{u_0 x/2\nu} E\left(\dfrac{x+u_0 t}{2\sqrt{\nu t}}\right) + e^{-u_0 x/2\nu} E\left(\dfrac{x-u_0 t}{2\sqrt{\nu t}}\right)}{2\cosh\dfrac{u_0 x}{2\nu} + e^{u_0 x/2\nu} E\left(\dfrac{x+u_0 t}{2\sqrt{\nu t}}\right) - e^{-u_0 x/2\nu} E\left(\dfrac{x-u_0 t}{2\sqrt{\nu t}}\right)}, \end{aligned} \tag{3.3}$$

where $E(x)$ denotes the error function

$$E(x) = \operatorname{erf}(x) = \frac{2}{\sqrt{\pi}} \int_0^x e^{-t^2}\, dt. \tag{3.4}$$

We can obtain u_x directly from (3.3) by differentiation, or we can simply use (3.2) to get

$$u_x(x, t) = -2\nu \frac{\phi_{xx}\phi - \phi_x^2}{\phi^2}, \tag{3.5}$$

where ϕ is the denominator in (3.3). ϕ_x, which can be extracted from the numerator of (3.3), needs to be differentiated once (we omit the details), and subsequent substitu-

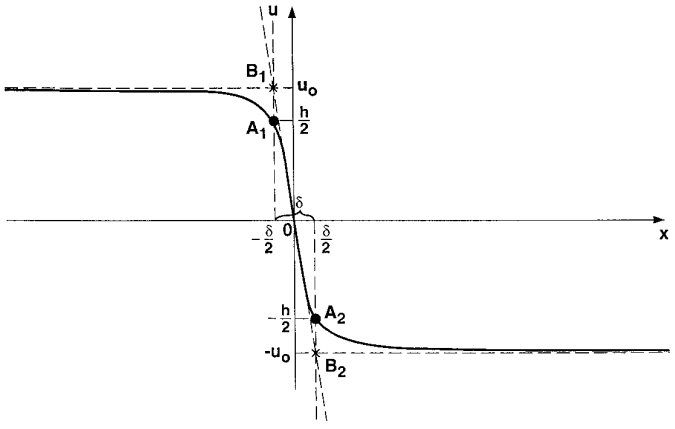

FIG. 1. Geometrical definition of shock width δ.

tion of ϕ, ϕ_x, and ϕ_{xx} into (3.5), along with setting $x = 0$, finally yields

$$u_x(0,t) = -u_0\left[\frac{u_0}{2\nu} + 1/\sqrt{\pi\nu t}\, e^{u_0^2 t/4\nu}\left[1 + E\left(\frac{u_0 t}{2\sqrt{\nu t}}\right)\right]\right]. \tag{3.6}$$

Note that from Fig. 1 it is clear that $x = 0$ is the global maximum point for $|u_x|$; this can be also derived by lengthy but straightforward differentiation of (3.5). We now proceed to give a more precise definition of the shock width.

3.2. The Shock Width

Although there are several definitions of shock width, in all of them the width is proportional to the ratio of the coefficient of viscosity (ν) and the shock strength ($2u_0$) [17]. For our purposes we define the shock as follows: draw the line going through the origin and having slope $u_x(0, t)$, and denote by B_1 and B_2 (Fig. 1) its intersection points with the asymptotes $u = u_0$ and $u = -u_0$, respectively. The sum of distances of points B_1 and B_2 to the $x = 0$ axis is then δ. The vertical lines $x = -\frac{1}{2}\delta$ and $x = \frac{1}{2}\delta$ will intersect the curve of $u(x, t)$ at points A_1 and A_2, which will be the previously mentioned "cutoff" points. So we are ultimately interested in how far points A_i, $i = 1, 2$, will move between two time steps.

Given the fact that most of the change in u due to the shock takes place within points A_1 and A_2, this definition certainly seems reasonable. Once $u_x(0, t)$ is known from (3.6), δ is also readily given (as a function of time) by

$$\delta(t) = \frac{2u_0}{|u_x(0,t)|} = 2\Big/\left(\frac{u_0}{2\nu} + 1/\sqrt{\pi\nu t}\, e^{u_0^2 t/4\nu}\left[1 + E\left(\frac{u_0 t}{2\sqrt{\nu t}}\right)\right]\right). \tag{3.7}$$

With respect to (3.7), we would like to point out the following.

Remark 3.1. When $t \to 0$ it follows that $\delta \to 0$, which confirms that initially we have jump discontinuity of width 0.

Remark 3.2. As $t \to \infty$, it implies $\delta \to 4\nu/u_0$, a result that can also be derived from the steady state solution

$$\lim_{t\to\infty} u(x,t) = -u_0 \tanh\frac{u_0 x}{2\nu} \tag{3.8}$$

by differentiating and setting $x = 0$. Moreover, if h denotes the vertical distance between points A_1 and A_2, then we can write using (3.8):

$$h = 2u_0 \tanh 1 \approx 0.761 \times 2u_0. \tag{3.9}$$

In other words, at steady state, the shock width yields the length over which about 76% of the change from left to right occurs.

3.3. The Travelling Wave Solution

To get a qualitative picture of the shock structure, it is sometimes useful to consider the travelling wave solution (e.g., [15]) $u(x, t) = u(\xi)$, $\xi = (x - st)/\nu$ of the more general version of (3.1),

$$u_t + f(u)_x = \nu u_{xx}, \tag{3.10a}$$

$$u(x,0) = \begin{cases} u_l, & \text{if } x < 0, \\ u_r < u_l, & \text{if } x \geq 0. \end{cases} \tag{3.10b}$$

The resulting ordinary differential equation in ξ can now be intergrated once to arrive at

$$-su + f(u) + c = u', \tag{3.11}$$

where s and c can be determined from "boundary conditions" $\lim_{\xi\to-\infty} u(\xi) = u_l$ and $\lim_{\xi\to\infty} u(\xi) = u_r$:

$$c = su_l - f(u_l), \tag{3.12a}$$

$$s = \frac{f(u_r) - f(u_l)}{u_r - u_l}, \tag{3.12b}$$

where the wave speed s is now identified as the shock speed, having the same expression as in the purely hyper-

bolic case. One more integration of (3.11) gives an implicit formula for u,

$$\int \frac{du}{f(u) - su + c} = \xi + c_1, \tag{3.13}$$

c_1 being a constant of integration. In the particular case of $f(u) = \frac{1}{2}u^2$ we obtain

$$u(\xi) = u_r \tanh \frac{u_l - u_r}{4}\xi. \tag{3.14}$$

When $u_l = -u_r = u_0$ as in (3.1b), (3.14) will also lead to (3.8).

The shock will therefore move with speed s and will tend to the quasi-steady profile of (3.14). Thus, the exact solution (3.3) can be modified to fit the more general initial data (3.10b) by simply substituting $x - ((u_l + u_r)/2)$ for each x and $(u_l - u_r)/2$ for each u_0 in (3.3). The interpretation of $2u_0$ in identities (3.6) and (3.7) is that of the shock strength; hence both formulae remain unchanged.

The shock width gives us an idea of how large the region of irregularity is at any given time. The change in shock width, $\Delta\delta$, on the other hand, indicates how far the irregularity would move during one time step, which is the information we need for the multiresolution analysis. Again, intuitively, it seems clear—and it is shown in Appendix A—that δ will change the most during the first time step, i.e., between $t = 0$ and $t = \Delta t$. The critical time step therefore is the first one, which will give us an upper bound on the possible change in δ:

$$D = \sup_{t>0} \Delta\delta(t) = \sup_{t>0} [\delta(t + \Delta t) - \delta(t)] = \delta(\Delta t). \tag{3.15}$$

4. TIME STEP RESTRICTION

In order to determine how many cells the shock will cut across during one time step, we now have (3.15) and (3.7), but to be useful, (3.7) needs to be further simplified. As in the purely hyperbolic case where the assumption of a CFL number less than unity was used (see [7, 2]), here too we can use the stability limitation on Δt. To derive a time step limitation, we may want to approach the problem from the linear point of view, where a classical von Neumann stability analysis can be applied to the sufficiently simplified scheme, or, on the nonlinear level, try to find conditions for total variation stability, a concept introduced by Harten [8]. In this section we shall use both of these stability methods and come up with reasonable linear *and* nonlinear stability estimates.

4.1. Linear Stability Analysis

Rigorous stability analysis, in the classical sense, can be done only for the linear flux (2.2a), which is the case we shall study in this subsection. Our aim is to derive some sufficient conditions for linear stability using periodic boundary conditions. In the case of a second-order ENO scheme, we altogether have four possibilities for the right-hand side of (2.7) for each j. If we consider only one of these cases and assume that it holds for all j simultaneously, we get stability conditions for this fixed stencil scheme. In other words, it is possible that the ENO scheme will choose the same orientation of stencil for each cell, and we argue that for the ENO scheme (2.11) to be stable, in the strict sense, the chosen special case must be stable as well.

Method for Stability Analysis

If the function M in (2.11c) always chooses the right-hand stencil for reconstruction, we can write using (2.11a):

$$v^-_{j+1/2} = \frac{v_{j+1} + v_j}{2} \tag{4.1}$$

and if this value is used as u_l in (2.9) and (2.8), the scheme (2.7) becomes

$$(v_j)_t = -\frac{1}{\Delta x}\left[\frac{a}{2}(v_{j+1} - v_{j-1}) - \frac{\nu}{\Delta x}(v_{j+1} - 2v_j + v_j - 1)\right]. \tag{4.2}$$

Equation (4.2), however, is nothing but the well-known *finite difference* scheme with central spatial discretization in a semi-discrete form.

There already exist stability results using first-order (Euler) time update for (4.2) (see [10, 12, 14]); but to get second-order accuracy in time also, we used the RK2 method (2.10). To analyze the stability of this combined scheme, we proceed as in the matrix method. (The matrix method's main advantage lies in its ability to handle arbitrary boundary conditions; although it has been pointed out in [10, 12] that in some cases it gives stability regions larger than the correct one. Because of the periodic boundary conditions, in our case, this method is equivalent to using von Neumann stability analysis.)

First, note that (4.2) can be written

$$\mathbf{v}' = A\mathbf{v}, \tag{4.3a}$$

where

$$\mathbf{v} = (v_0, v_1, ..., v_{N-1})^{\mathrm{T}} \tag{4.3b}$$

and

$$A = -\frac{1}{\Delta x}\begin{pmatrix} \frac{2\nu}{\Delta x} & \frac{a}{2}-\frac{\nu}{\Delta x} & 0 & \cdots & 0 & -\frac{a}{2}-\frac{\nu}{\Delta x} \\ -\frac{a}{2}-\frac{\nu}{\Delta x} & \frac{2\nu}{\Delta x} & \frac{a}{2}-\frac{\nu}{\Delta x} & \cdots & 0 & 0 \\ 0 & -\frac{a}{2}-\frac{\nu}{\Delta x} & \frac{2\nu}{\Delta x} & \cdots & 0 & 0 \\ \vdots & \vdots & \vdots & & \vdots & \vdots \\ 0 & 0 & 0 & \cdots & \frac{2\nu}{\Delta x} & 0 \\ \frac{a}{2}-\frac{\nu}{\Delta x} & 0 & 0 & \cdots & -\frac{a}{2}-\frac{\nu}{\Delta x} & \frac{2\nu}{\Delta x} \end{pmatrix}. \tag{4.3c}$$

Matrix A is a circulant matrix, and, as such, its eigenvalues are given by [16]

$$\lambda_j = -\frac{2\nu}{(\Delta x)^2} + \frac{2\nu}{(\Delta x)^2}\cos\frac{2\pi j}{N} - i\frac{a}{\Delta x}\sin\frac{2\pi j}{N}, \tag{4.4}$$

where $j = 0, ..., N-1$. To simplify the algebra and clarify the meaning of the variables, we introduce

$$\sigma = \frac{a\Delta t}{\Delta x}, \tag{4.5a}$$

$$R = \frac{a\Delta x}{\nu}. \tag{4.5b}$$

Here σ corresponds to the usual CFL number, and R is the mesh Reynolds number. Also, for brevity, we let

$$c = \cos\frac{2\pi j}{N}, \tag{4.5c}$$

so that (4.4) becomes

$$\lambda_j = \frac{1}{\Delta t}\left[-2\frac{\sigma}{R}(1-c) - i\sigma\sqrt{1-c^2}\right]. \tag{4.6}$$

Returning to Eq. (4.3a), we diagonalize its coefficient matrix A,

$$A = T^{-1}\Lambda T,$$

$$\Lambda = \mathrm{diag}(\lambda_j)$$

and set

$$\mathbf{w} = T\mathbf{v}.$$

Then (4.3a) is equivalent to

$$\mathbf{w}' = \Lambda\mathbf{w}. \tag{4.7}$$

When integrating each (now uncoupled) equation of (4.7) by a numerical method

$$w_j^{n+1} = \kappa(\lambda_j\Delta t)w_j^n,$$

we say that the method is stable if the amplification factor κ satisfies

$$|\kappa(\lambda_j\Delta t)| \le 1 \tag{4.8}$$

for each $j = 0, ..., N-1$. Matrix A is circulant, hence normal; thus T is orthonormal, so stability for w is equivalent to stability for v (their L_2-norms are equal). This reasoning is general enough that it holds for all ODE time-integration methods; we shall use it for RK2.

Approximate Region of Stability

The amplification factor κ for the RK2 method is given by (e.g., [4])

$$\kappa(\lambda\Delta t) = 1 + \lambda\Delta t + \tfrac{1}{2}(\lambda\Delta t)^2. \tag{4.9}$$

When λ_j (4.6) is used in (4.9), we get a quite complicated expression for $|\kappa|$ and inequality (4.8) will not have a closed form solution. Although numerical stability regions are always available, for the purposes of this paper we seek a

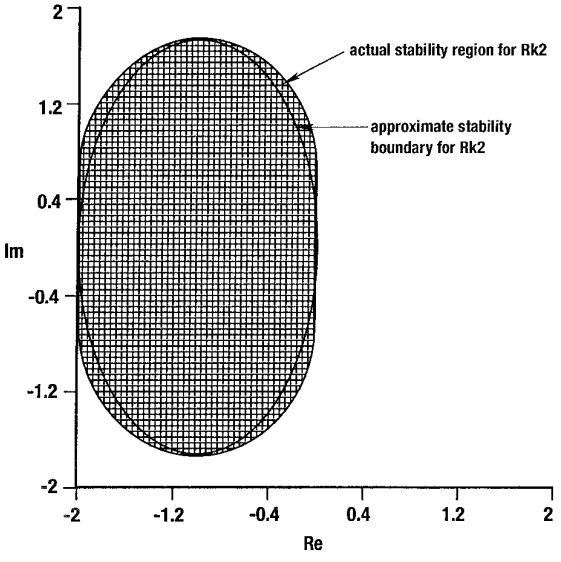

FIG. 2. Exact and approximate stability regions in the complex $\lambda\Delta t$ plane.

bound on Δt to be used in (3.7). We have experimented with algebraic ways to obtain solutions of (4.8), but the calculations were lengthy and cumbersome, and finally they gave only sufficient conditions. We then came up with the following geometric (and more intuitive) argument. Knowing that the stability region of the RK2 method, when plotted in the complex $z = a + ib$ plane, is close to an ellipse, we propose to *approximate* this exact stability region by an ellipse, which, as it turns out (and is proved in Appendix B) is enclosed in the actual region of stability (see Fig. 2) and touches it at four points. Thus the ellipse's major and minor axes are $2\sqrt{3}$ and 2 long, respectively, and its center is located at $(-1, 0)$. Instead of (4.8), we now require

$$[\mathrm{Re}(\lambda\Delta t) + 1]^2 + \tfrac{1}{3}[\mathrm{Im}(\lambda\Delta t)]^2 \le 1. \tag{4.10}$$

Upon substitution of (4.6) into (4.10), we arrive at

$$\left[-\frac{2\sigma}{R}(1-c)+1\right]^2 + \frac{1}{3}\sigma^2(1-c^2) \le 1 \tag{4.11}$$

which must hold for all $-1 \le c \le 1$. After simplification (details omitted), we are left with two conditions that $\sigma = \sigma(R)$ has to obey:

$$\sigma \le \frac{R}{2} \tag{4.12a}$$

and

$$\sigma \le \frac{6}{R}. \tag{4.12b}$$

By (4.5a)–(4.5b), conditions (4.12) translate into the condition on the time step:

$$\Delta t \le \min\left(\frac{6\nu}{a^2}, \frac{(\Delta x)^2}{2\nu}\right). \tag{4.13}$$

Figure 3 shows this region in the $\sigma - R$ plane.

Remark 4.1. For the RK1 method (forward Euler) we have a similar but more restrictive result (see [10]),

$$\Delta t \le \min\left(\frac{2\nu}{a^2}, \frac{(\Delta x)^2}{2\nu}\right). \tag{4.14}$$

(See Fig. 3 for a comparison with (4.13).)

Remark 4.2. Note that $R \to \infty$ represents the inviscid case ($\nu \to 0$) for which both the RK1 and RK2 methods are unconditionally unstable when used with central differencing in space.

4.2. Stability Analysis on the Nonlinear Level

We now turn to analyze the total variation stability of the numerical scheme. The following analysis will apply to linear or nonlinear fluxes, and the second order in space, first order in time, *nonlinear* total variation diminishing (TVD) scheme; the only difference between this and the (first-order in time) ENO scheme is the definition of the function M (2.11c). For the TVD scheme the minmod

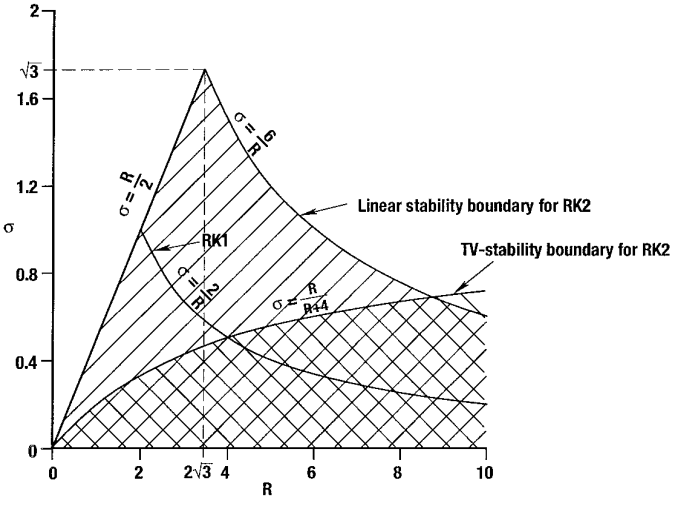

FIG. 3. Linear and nonlinear stability boundaries in the σ-R plane.

function is used instead, which simplifies to (2.11c) if the signs of a and b are the same. In most of the domain (except for local extrema) the two schemes will, in fact, be identical. The stability bound will then be extended, using the Shu–Osher result [21], to the TVD scheme which is of second-order temporal accuracy. Using the previous reasoning, this CFL condition will be used for the ENO scheme also.

A scheme (2.4) is said to be *total variation stable* if the total variation (TV)

$$\mathrm{TV}(v_h(x,t)) = \mathrm{TV}(v^n) = \sum_{j=0}^{N-1} |v_{j+1}^n - v_j^n| \tag{4.15}$$

of a sequence of numerical approximations $v_h(x, t)$ is uniformly bounded in $h = \Delta x$ and $t = n\Delta t$, with $h \to 0$ and $0 \le t \le T$ (see [8]). Moreover, the scheme is *total variation diminishing* (TVD) if

$$\mathrm{TV}(v^{n+1}) \le \mathrm{TV}(v^n). \tag{4.16}$$

Clearly, a TVD scheme is total variation stable.

Using these definitions, Harten shows the following in [8].

LEMMA 4.1. *If a scheme written in the form*

$$v_j^{n+1} = v_j^n + C_j^+ \Delta_+ v_j^n - C_{j-1}^- \Delta_- v_j^n, \tag{4.17}$$

where $\Delta_+ z_j = z_{j+1} - z_j$, $\Delta_- z_j = z_j - z_{j-1}$, *satisfies, for all* j,

$$C_j^+ \ge 0, \tag{4.18a}$$

$$C_j^- \ge 0, \tag{4.18b}$$

$$C_j^+ + C_j^- \le 1, \tag{4.18c}$$

then the scheme is TVD.

He then introduces the following explicit scheme, with first- and second-order spatial and first-order temporal accuracy,

$$v_j^{n+1} = v_j^n + \hat{C}_j^+ \Delta_+ v_j^n - \hat{C}_j^- \Delta_- v_j^n, \tag{4.19a}$$

$$\hat{C}_j^{\pm} = \tfrac{1}{2}\left[|\omega + \zeta| \mp (\omega + \zeta)\right]_j, \tag{4.19b}$$

$$\omega_j = \lambda \frac{\Delta_+ f_j}{\Delta_+ v_j} \tag{4.19c}$$

$$\zeta_j = \frac{\Delta_+ g_j}{\Delta_+ v_j}, \tag{4.19d}$$

where $f_j = f(u_j)$; moreover, $g_j = g(v_j)$ is chosen so that

$$|\zeta_j| \le \rho(\omega_j) \tag{4.20a}$$

with

$$\rho(a) = \begin{cases} 0 & \text{for first order in space} \\ \frac{1}{2}(|a| - a^2) & \text{for second order in space.} \end{cases} \tag{4.20b}$$

In the above and throughout this section we omit the superscripts n wherever its meaning is obvious. With these definitions, Harten shows that for both the first- and second-order schemes (4.19)–(4.20), a sufficient condition for the scheme to be TVD is a CFL-like condition

$$\max_j |\omega_j| \le 1, \tag{4.21}$$

since ω_j, as defined by (4.19c), is the mean-value local CFL number. We shall now revisit the proof given for the second-order case and modify it to account for the added viscosity. First, we state the result.

THEOREM 4.2. A scheme of the form (4.17), with $C_j^{\pm}$ defined by

$$C_j^{\pm} = \hat{C}_j^{\pm} + \lambda \frac{\nu}{\Delta x}, \tag{4.22}$$

where $\hat{C}_j^{\pm}$ comes from definition (4.19b), is TVD if

$$\sigma \le \frac{R}{R+4} \tag{4.23}$$

with σ and R given by

$$\sigma = \max_j |\omega_j|, \tag{4.24a}$$

$$R = \max_j |\omega_j| \frac{\Delta x}{\lambda \nu}. \tag{4.24b}$$

Remark 4.3. We observe that the scheme (4.17), (4.22) approximates (2.1a) to second order in space, since we added a second order, centrally discretized viscous term to Harten's original second-order TVD scheme.

Remark 4.4. The definition of σ and R is somewhat different from that of the linear stability analysis, but their qualitative meaning is the same; (4.24a)–(4.24b) are the nonlinear equivalents of (4.5a)–(4.5b).

Proof of Theorem 4.2. We shall prove this theorem by showing that the conditions of Lemma 4.1 are satisfied. With the definitions of $\hat{C}_j^{\pm}$ given in [8], conditions (4.18a)–(4.18b) are immediately satisfied. Once (4.18c) is shown, the theorem itself is proven. We need to show therefore:

$$\hat{C}_j^+ + \hat{C}_j^- + 2\lambda \frac{\nu}{\Delta x} \le 1. \tag{4.25}$$

With definitions (4.19b)–(4.19d), (4.20b), and (4.24a)–(4.24b), and property (4.20a), it follows that (4.25) will be satisfied if

$$\frac{3}{2}\sigma - \frac{1}{2}\sigma^2 + 2\sigma\frac{1}{R} \le 1. \tag{4.26}$$

Since

$$\sigma\frac{4}{R}(\sigma - 1) \le 0 \tag{4.27}$$

($\sigma \le 1$ is required by (4.20a)), a slightly more restrictive version of (4.26) would be obtained by adding (4.26) and (4.27) to get

$$(\sigma - 2)\left[\sigma\left(1 + \frac{4}{R}\right) - 1\right] \ge 0. \tag{4.28}$$

It is now evident that (4.28) is satisfied if

$$\sigma \le \frac{R}{R+4},$$

which completes the proof. ∎

Remark 4.5. The slight strengthening of the stability bound (4.26) by (4.27) is very small. By solving the quadratic inequality (4.26) directly, it is possible to get a bound for (4.26) which is quite complicated, and it deviates from the approximate one by a negligible amount; both approach 1 and $R \to \infty$. Strictly speaking, therefore, the theorem gives *sufficient* conditions for TV-stability. However, our numerical experiments indicate that, for all practical purposes, (4.23) is also a *necessary* condition.

Since Theorem 4.2 holds for first-order time update only, we invoke a result by Shu and Osher [13] that relates first order in time TVD schemes to TVD schemes with higher order time updates. In particular, it is shown in [13], that if the Heun method (2.10) (one form of RK2) is used to advance the solution in time, the resulting method will be TVD if the corresponding first-order (in time) method is TVD (i.e., both subject to the same CFL-like restriction). As it applies to our case, we conclude that the scheme (2.10), with S_j given by

$$S_j = \frac{1}{\Delta x}(C_j^+ \Delta_+ v_j^n - C_j^- \Delta_- v_j^n), \tag{4.29}$$

is TVD and, therefore, TV-stable if (4.23) is satisfied. Finally, we note that the original ENO scheme is expected to be stable as well, under the same CFL-like restrictions. In the absence of rigorous theory for the ENO scheme, for the second-order case we use its similarity to the TVD scheme to support the above conjecture; all of our numerical experiments also support this claim.

5. THE MULTIRESOLUTION SCHEME

In this section we combine the numerical scheme presented in Section 2 with the multiresolution algorithm used for regularity analysis, introduced in [7]. After briefly reviewing the original algorithm, we present the modification necessary for it to work in the viscous case.

5.1. A Review of Harten's 1D Multiresolution Analysis

We first briefly review Harten's 1D multiresolution scheme [7] and its semi-discrete implementation, first presented in [1] (in this work we use the version that is referred to in [1] as "full multiresolution scheme"). These references contain ample detail with regard to both analysis and actual algorithm in a form of pseudo-code; we refer the reader to these sources. The 1D multiresolution modules can also be considered special cases of the 2D algorithms presented in [2]. The main steps of the algorithm now follow.

We compute the multiresolution representation $\overline{v}_{\mathbf{M}}^n$ of the cell averages v_j^n of the solution at time step n,

$$\overline{v}_{\mathbf{M}}^n = (d^1, d^2, ..., d^L, \overline{v}^L)^{\mathrm{T}}, \tag{5.1}$$

$$\overline{v}_{\mathbf{M}}^n = \mathbf{M} v^n, \tag{5.2}$$

where the d^k are the scale or *multiresolution* coefficients and $\overline{v}^L$ is the cell average array on the coarsest grid corresponding to level L. This procedure, the "encoding" $\mathbf{M}$, gives much information about the regularity of the function v. The size of the coefficients d^k, among other things, can be used to predict our success in obtaining the fluxes $\bar{f}_{j+1/2}$ from coarser levels by central interpolation, instead of the direct flux computation of (2.8). The d's that fall below a certain prescribed tolerance are truncated to zero; these are the localities where interpolation from the next coarser level is accurate enough. Everywhere else the fluxes must actually be evaluated.

For the direct flux computations, we also need the approximate values of the cell averages v, obtained by the "decoding" using the truncated values of the d's. Symbolically, this corresponds to an operation $\mathbf{M}^{-1}$ (since our multiresolution interpolation uses a fixed stencil, $\mathbf{M}$ and $\mathbf{M}^{-1}$ are constant matrices);

$$\tilde{v}^n = \mathbf{M}^{-1}\hat{v}^n, \tag{5.3}$$

with

$$\hat{v}^n = \mathbf{tr}(\overline{v}^n_{\mathbf{M}}), \tag{5.4}$$

where **tr** is the aforementioned truncation operation.

The numerical flux computations start on the coarsest level L, where the fluxes are evaluated directly using (2.8). On each level thereafter a decision is made at each cell face whether to compute the flux directly or to interpolate. Once the fluxes on the finest level are all computed, we are ready to perform the first stage of a second-order Runge–Kutta (RK2) time stepping on the finest grid. The entire procedure then repeats for the second stage of the RK2 method.

The algorithm can be summarized in operator form as (to be carried out in a right-to-left order)

$$v_j^{n+1} = \overline{\mathbf{E}}^{(1)}_{\mathbf{M}}\mathbf{M}^{-1}\mathbf{trM}\,\overline{\mathbf{E}}^{(0)}_{\mathbf{M}}\mathbf{M}^{-1}\mathbf{trM}v^n, \tag{5.5}$$

where $\overline{\mathbf{E}}^{(0)}_{\mathbf{M}}$ and $\overline{\mathbf{E}}^{(1)}_{\mathbf{M}}$ are the two-stage equivalents of the evolution operator $\overline{\mathbf{E}}_{\mathbf{h}}$ in (2.4).

The truncation operation above actually includes the regularity analysis, the heart of a multiresolution scheme. The regularity analysis is the systematic comparison of the size of the multiresolution coefficients to the allowable tolerance ε_k, performed at each level $0 < k \le L$. It is at this step where the decision, whether to compute directly or to interpolate from coarser levels, is made. Wherever the coefficients d^k fall below the tolerance, interpolation is sufficient; otherwise we need to compute as usual. The more we can truncate, the more exact flux evaluations and ENO reconstructions we save.

In the above algorithm it was also important to account for the possible movement of an irregularity, since from the current location of a shock we will not get the correct future shock unless the cell that would contain it at the next time step is solved for exactly also. For hyperbolic problems we assumed finite speed of wave propagation, along with a CFL number less than one, resulting in a ''padding'' of one cell to the left and one cell to the right of the current shock location.

The algorithm can be used, with a relatively minor modification, for the numercial solution of conservation laws with viscosity. The only assumption not valid here is that of the finite wave speed. However, once we can reliably predict the shock movement, the rest of the multiresolution scheme can be used unchanged.

5.2. The Multiresolution Stencil

We now turn to combine results from Sections 3 and 4 in order to estimate the amount by which the region of irregularity must be enlarged to account for the movement of the shock from the current time step to the next. We shall concentrate on the nonlinear case, so we shall use the shock width results from Section 3; but in the absence of theory on stability (or convergence) for ENO schemes, we shall make the usual leap, from proving linear or nonlinear stability for a slightly simplified scheme, to conjecturing stability for *our* scheme.

We start by defining the nonlinear versions of σ and R:

$$\sigma_u = \frac{u\Delta t}{\Delta x}, \tag{5.6a}$$

$$R_u = \frac{u\Delta x}{\nu}. \tag{5.6b}$$

From (5.6a) we get

$$\Delta t = \frac{\sigma_u \Delta x}{u}, \tag{5.7}$$

which, when evaluated at u_0 and substituted into (3.7) gives (after simplification and omission of the u_0 subscript from σ and R):

$$\delta(\Delta t) = 2\Delta x \Big/ \left\{\frac{R}{2} + \sqrt{\frac{R}{\pi\sigma}}\,1/e^{\sigma R/4}\left[1 + E\left(\frac{\sqrt{\sigma R}}{2}\right)\right]\right\}. \tag{5.8}$$

We shall now derive upper limits for the shock widening in the linear and nonlinear cases, using stability conditions (4.12) and (4.23), respectively. Our goal is estimate the extent of shock widening in terms of R.

Estimate Using the Linear Stability Bound

If we use the definitions (4.5a) and (4.5b) for σ and R in (5.8), respectively, then application of (4.12b) in the second term of the denominator of (5.8) gives

$$\delta(\Delta t) \le 2\Delta x \Big/ \left\{\frac{R}{2} + \sqrt{\frac{R}{\pi\sigma}}\,1/e^{3/2}\left[1 + E\left(\sqrt{\frac{3}{2}}\right)\right]\right\}. \tag{5.9}$$

For simplicity, introduce the constant

$$\alpha = \sqrt{\pi}\,e^{3/2}\left[1 + E\left(\sqrt{\frac{3}{2}}\right)\right] \approx 15.216 \tag{5.10}$$

so that (5.9) becomes

$$\delta(\Delta t) \le 2\Delta x \Big/ \left(\frac{R}{2} + \sqrt{\frac{R}{\sigma}}\frac{1}{\alpha}\right). \tag{5.11}$$

To find out how many cells P the shock will span at time Δt, we must equate the left-hand side of (5.11) to $P\Delta x$

and express P, an integer, from it. We now use stability condition (4.12a) to get the following general form for P:

$$P \le 2 \Big/ \left[\frac{R}{2} + \sqrt{\frac{R}{\min(R/2, 6/R)}} \frac{1}{\alpha} \right]. \tag{5.12}$$

We have now arrived at an expression for the measure of stencil size which is useful; R is the only variable here and (5.12) needs to be evaluated only in the regions of the finest grid where exact computations are needed. P being an integer, we must decide exactly how we interpret the right-hand side of (5.12). One approach is to take its integer part and add one, to ensure we "are on the safe side." Our numerical experiments show that rounding is sufficient; i.e., if the right-hand side expression is below $I + \frac{1}{2}$, then $P = I$; otherwise $P = I + 1$, I being an integer.

A closer look at (5.12) can reveal its other favorable properties. In particular, we may be interested to find out for what values of R is $P \le \frac{1}{2}$ (assuming rounding is used) so that we need no stencil enlargement beyond the one required by the shock convection. (The travelling wave solution of Section 3.3 shows that the shock speed is the same as in the inviscid case.) In order to do this, we explicitly discuss the two cases implied by the minimum operation in (5.12):

(i) If $R/2 \le 6/R$, then $R \le 2\sqrt{3}$, and we require

$$4\left(R + \frac{2\sqrt{2}}{\alpha} \right) \le \frac{1}{2}. \tag{5.13}$$

(5.13) holds for all R satisfying

$$2\left(4 - \frac{\sqrt{2}}{\alpha} \right) \le R \le 2\sqrt{3}$$

which, considering the value of α from (5.10), is impossible.

(ii) On the other hand, if $R/2 > 6/R$, then $R > 2\sqrt{3}$, and the condition of R is

$$2 \Big/ \left[R\left(\frac{1}{2} + \frac{1}{\alpha\sqrt{6}} \right) \right] \le \frac{1}{2}, \tag{5.14}$$

or

$$R \ge 4 \Big/ \left(\frac{1}{2} + \frac{1}{\alpha\sqrt{6}} \right) \approx 7.593. \tag{5.15}$$

That is, as long as R obeys (5.15), there is no additional stencil enlargement needed due to the viscous term.

Estimate Using the Nonlinear Stability Bound

If the total variation stability bound (4.23) is used in conjunction with identity (5.8), we argue as follows. First, we can simplify (5.8) by noting that $E(x) < 1 \ \forall x \ge 0$; then we apply (4.23) to arrive at an expression for the number of cells P that the shock may occupy,

$$P \le 4 \Big/ \left[R + \sqrt{\frac{R+4}{\pi}} e^{-R^2/[4(R+4)]} \right]. \tag{5.16}$$

As in the linear stability case, it is useful to find conditions on R for which $P \le \frac{1}{2}$, so that the multiresolution stencil does not need to be extended due to the viscosity term. In this case, this special condition amounts to requiring

$$R + \sqrt{\frac{R+4}{\pi}} e^{-R^2/[4(R+4)]} \ge 8, \tag{5.17}$$

which, using a numerical root finder, is satisfied whenever

$$R > 7.4297. \tag{5.18}$$

Remark 5.1. A comparison of (5.15) to (5.18) reveals that both the linear and nonlinear stability bounds give similar regions where a "hyperbolic" multiresolution stencil is adequate. This stems from the two stability curves being close to each other in the neighborhood of $R = 8$, as seen from Fig. 3 also.

Remark 5.2. Even when $R \to 0$ and we expect a very wide (and weak) shock, (5.8) implies, in both the linear and nonlinear cases, that P is finite,

$$P \le 2\sqrt{\pi} \approx 3.545, \tag{5.19}$$

which is, in fact, its supremum over all $R > 0$.

As it is known from the theory, two competing forces are present in Burgers' equation: nonlinearity which tries to keep the shock sharp, and viscosity which attempts to smooth it. When the shock is wide, we may be forced to overresolve it by enlarging the multiresolution stencil by possibly several points; but at the next time step the solution may become so smooth that there is no need for any exact computations in the neighborhood of what used to be a sharp shock. This special treatment due to viscosity is used only near cells where the multiresolution analysis finds some irregularity. If the irregularity is smoothed out, no multiresolution stencil extension is needed, since there *is no* stencil.

6. NUMERICAL RESULTS IN THE 1D VISCOUS CASE

We now present several sets of numerical results for both the linear and nonlinear cases, for various values of R and different initial conditions, but for the same grid of 256 points on the finest level and periodic boundary conditions in all cases. Since the numerical scheme used in both the linear and nonlinear fluxes was the nonlinear ENO scheme, we used a time step restriction corresponding to the CFL-like condition (4.23):

$$\sigma = \frac{R}{R+4} \tag{6.1}$$

$$\Delta t = \sigma \frac{\Delta x}{u_{\max}}. \tag{6.2}$$

For the same reasons, we used inequality (5.16) for the parameter P (defined in Section 5), instead of (5.12).

In all computations we used $\varepsilon = 10^{-3}$, as the multiresolution tolerance, and $L = 5$ levels. As a measure of the "speedup" achieved using multiresolution analysis we adopted the *efficiency* μ defined in [7] as

$$\mu = \frac{N_0}{N_0/2^L + |D^n|},$$

where D^n is the set of those cells, on all multiresolution levels, at time n, where exact computations are required by the regularity analysis. The errors e_1, e_2, and e_∞ are the l_1, l_2, and maximum norms, respectively, of the differences between the multiresolution solution and the classical or non-multiresolution solution.

For each case we plotted the solution (part "(a)" of the figure) and the corresponding multiresolution diagram (part "(b)"). The multiresolution diagram contains a symbol wherever large regularity coefficients occur in the $x - l$ plane, where $l, 0 \le 1 \le L = 5$ is the level of resolution (the grid coarsens as l increases). Namely, the circles indicate exact flux computation and ENO reconstruction.

6.1. The Linear Case

When (2.2a) is used with $a = 1$ and the unit step function

$$u_0(x) = \begin{cases} 1, & \text{if } -1 \le x \le 0, \\ 0, & \text{if } 0 < x < 1, \end{cases} \tag{6.3}$$

as the initial condition, we get an idea of how the multiresolution scheme performs with a linearly moving and nonsharpening discontinuity. Four runs were done, holding all parameters constant except R:

(i) $R = 0.001$. This is the smallest mesh Reynolds number we have used in computations, and it corresponds to a very viscous case, and, thus, a relatively high value of P: $P \approx \text{int}(3.54) = 4$, where we use "int($x$)" to denote the *rounded* integer representation of a real number x. After 1000 time steps, but at t only 0.00195, we get the profile shown in Fig. 4a. The corresponding multiresolution diagram of Fig. 4b also confirms our expectation of a quick smoothing process where two of the finest levels do not show any nonzero coefficients. An efficiency of 4.0 is reached at $n = 1000$ (Table I), after a transient stage where μ dips well below 3 because of the padding required by the viscous term. The errors, when compared to the non-multiresolution solution, are small, although they accumulate in time.

TABLE I

Numerical Solution of 1D Convection-Diffusion Equation, I.C. (6.3)

R	n	μ	e_1	e_2	e_∞
0.001	10	2.91	9.28×10^{-6}	3.57×10^{-5}	1.91×10^{-4}
	100	2.91	1.09×10^{-4}	1.91×10^{-4}	7.29×10^{-4}
	200	2.78	2.12×10^{-4}	3.38×10^{-4}	1.20×10^{-3}
	600	3.20	3.71×10^{-4}	4.64×10^{-4}	1.33×10^{-3}
	1000	4.00	6.41×10^{-4}	7.34×10^{-4}	1.67×10^{-3}[a]
0.1	10	2.91	9.67×10^{-6}	3.66×10^{-5}	2.32×10^{-4}
	100	2.46	1.04×10^{-4}	1.79×10^{-4}	6.41×10^{-4}
	200	2.72	2.03×10^{-4}	3.41×10^{-4}	1.25×10^{-3}[a]
	600	3.20	4.07×10^{-4}	4.91×10^{-4}	1.45×10^{-3}
	1000	4.00	6.51×10^{-4}	7.51×10^{-4}	1.80×10^{-3}
1	10	2.98	1.29×10^{-5}	3.61×10^{-5}	2.24×10^{-4}
	100	2.78	1.22×10^{-4}	2.12×10^{-4}	7.94×10^{-4}
	200	2.91	3.33×10^{-4}	4.92×10^{-4}	1.64×10^{-3}
	600	2.78	4.68×10^{-4}	5.97×10^{-4}	1.64×10^{-3}
	1000	3.28	7.81×10^{-4}	9.07×10^{-4}	1.96×10^{-3}[a]
10	10	3.28	3.23×10^{-5}	7.57×10^{-5}	4.26×10^{-4}
	100	2.37	1.58×10^{-3}	3.58×10^{-3}	1.33×10^{-2}
	200	2.42	1.49×10^{-3}	2.86×10^{-3}	1.39×10^{-2}
	600	2.78	6.91×10^{-3}	1.14×10^{-2}	3.61×10^{-2}[a]
	1000	2.91	9.41×10^{-3}	1.39×10^{-2}	3.81×10^{-2}

[a] A figure is enclosed for this particular case.

(ii) $R = 0.1$. This is a moderate mesh Reynolds number, where the multiresolution stencil enlargement needed is slightly smaller than the previous case ($P \approx \text{int}(3.22) = 3$). The transient efficiencies are similar to the previous cases, although the smoothing is much slower. See Table I and Figs. 5a,b.

(iii) $R = 1$. Here the CFL number is already at $\frac{1}{4}$, and the convective effect now dominates over the diffusive process (Fig. 6a). Again, the multiresolution diagram of Fig. 6b holds no surprises: the coefficients from the finest level have disappeared, and only a few exist on the second finest one. This case corresponds to $P \approx \text{int}(1.81) = 2$.

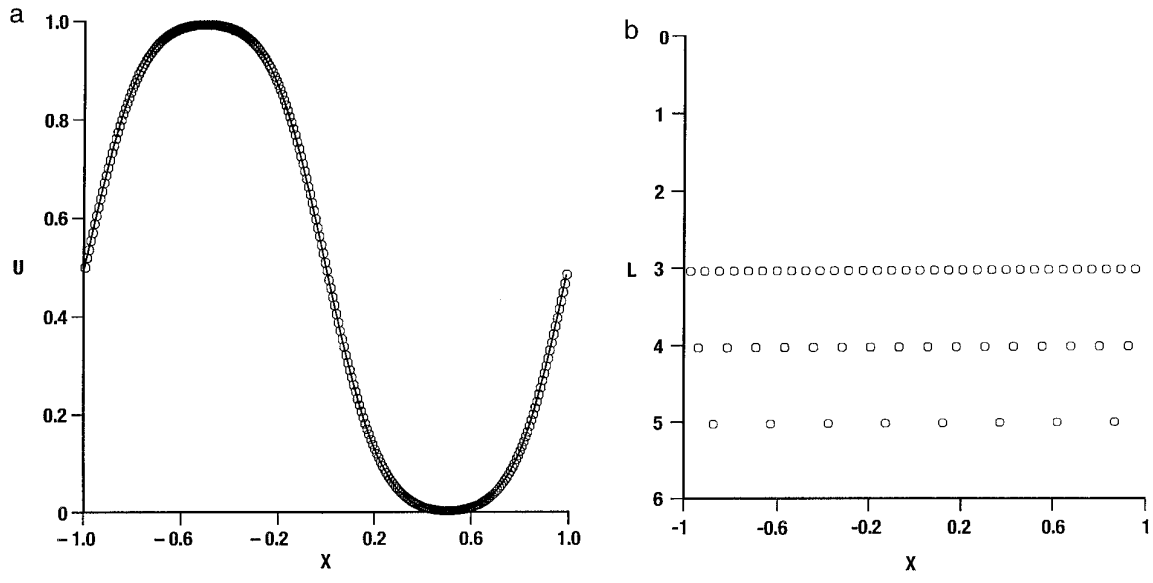

FIG. 4. Solution at $n = 1000$, $R = 0.001$, convection–diffusion equation, I.C. (6.3).

(iv) $R = 10$. This case is approaching the limiting case where the viscosity is very low, and the smoothing effect is correspondingly slow. There is no viscous stencil extension (according to (5.16), $P \approx \text{int}(0.39) = 0$), but the efficiency is still in the transient at $n = 1000$ (see Table I and Figs. 7a,b); and it will take a long time before it reaches the smooth stage of the earlier cases, which will happen more because of the numerical dissipation than the physical one. This case also serves as an example to show that (in both the linear and the nonlinear cases) the inviscid solution can be obtained by taking $\nu \to 0$. This numerical evidence reinforces some of the analysis indicating that the addition of multiresolution to the scheme changes neither the numerical nor the physical properties of the problem.

6.2. The Nonlinear Case

For the nonlinear problem we want to analyze the behavior of the multiresolution scheme for both discontinuous

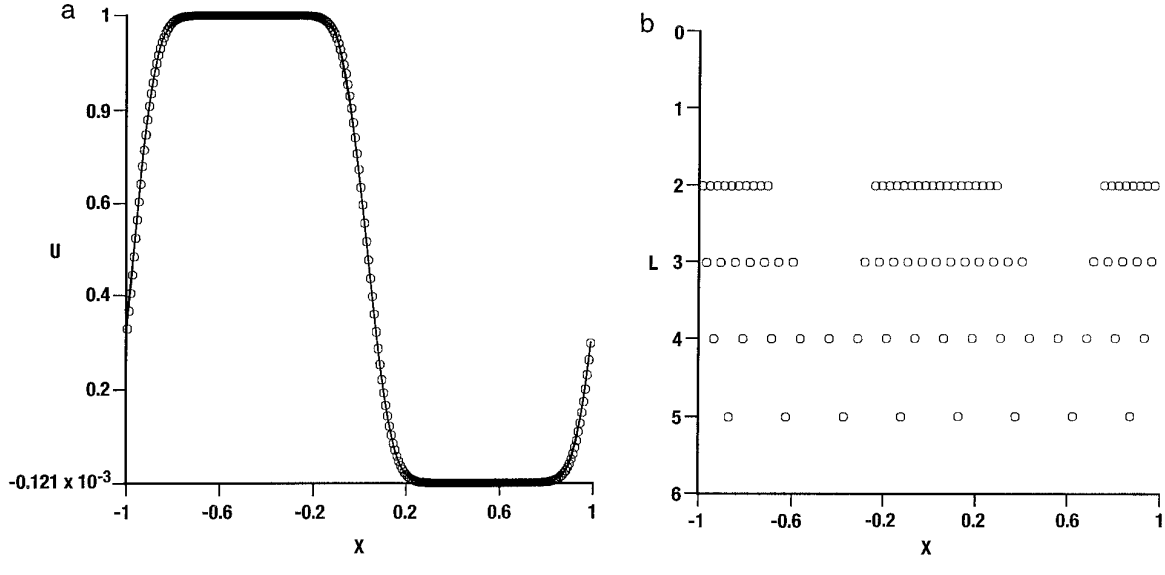

FIG. 5. Solution at $n = 200$, $R = 0.1$, convection–diffusion equation, I.C. (6.3).

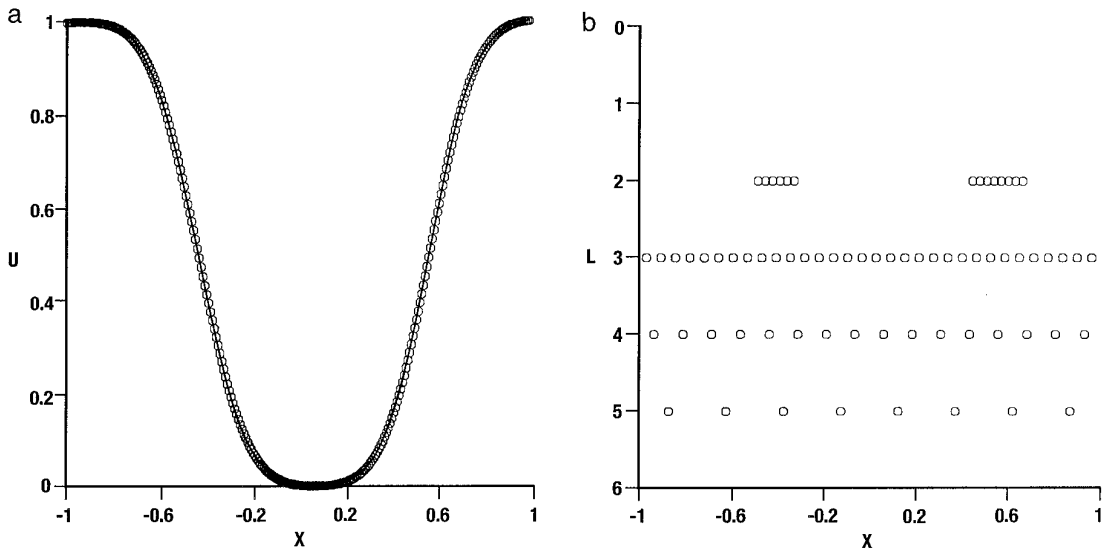

FIG. 6. Solution at $n = 1000$, $R = 1$, convection–diffusion equation, I.C. (6.3).

and smooth initial data. Both yield (although possibly weak) discontinuities after finite time, but they behave differently in the transient.

A. *Discontinuous Initial Data*

Using IC (6.3) and flux (2.2b), we show results for three values of R:

(i) $R = 0.001$. The solution as shown in Figs. 8a,b and Table II, is almost identical to its linear counterpart of Figs. 4a,b and Table I. The aforementioned balance between nonlinearity and viscosity is tilted much toward the latter, so that the convective part of the flux is negligible.

(ii) $R = 1$. On Fig. 9a one can clearly recognize the shock, although smeared, and the rarefaction, also smeared. The diagram on Fig. 9b shows some fine level cells for the shock, but the (smooth) corners of the rarefaction wave are represented only from the second finest level on. The efficiency is relatively high, being around 3, even in the transient. This mesh Reynolds number can be considered "moderate" also in the sense that both of the two competing forces are felt. As in the previous cases, the

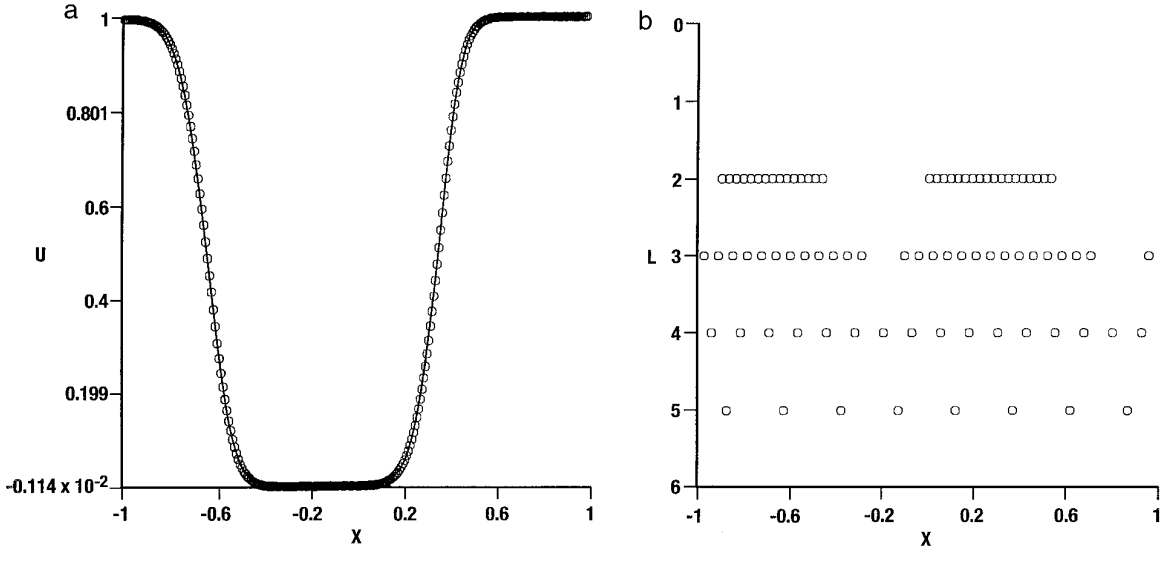

FIG. 7. Solution at $n = 600$, $R = 10$, convection–diffusion equation, I.C. (6.3).

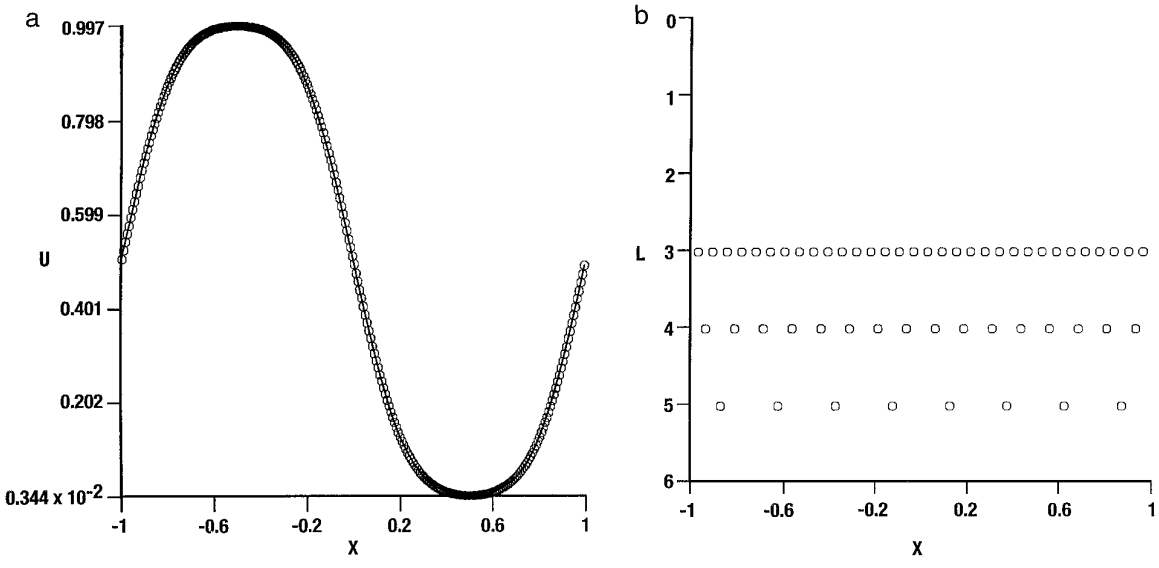

FIG. 8. Solution at $n = 1000$, $R = 0.001$, viscous Burgers' equation, I.C. (6.3).

errors, when compared to the non-multiresolution solution, stay quite small, ensuring that the behavior and quality of the solution are not altered.

(iii) $R = 10$. Here we expect an almost inviscid behavior. Indeed, when compared to corresponding results of [1], the efficiencies of Table II, the profile of Fig. 10a, and the diagram of Fig. 10b are similar to their inviscid counterparts. After a slight initial drop, μ steadily increases in time, since after 600 time steps it already shows a fully developed N-wave (Fig. 10a).

B. *Smooth Initial Data*

For this case we take the initial condition to be

$$u_0(x) = \sin(\pi x), \quad -1 \le x < 1. \tag{6.4}$$

Except for the limiting case when R is very large, in this case a fully discontinuous shock of width 0 never exists. Thus, the shock will never "widen," rather the opposite. We know from the physics that the generic estimate (3.15),

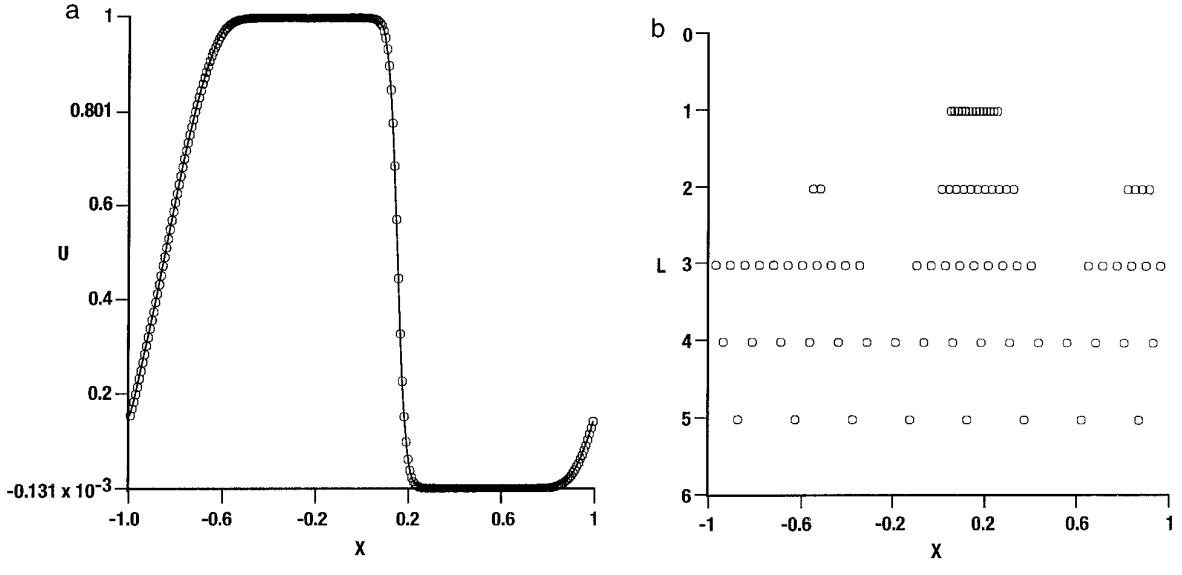

FIG. 9. Solution at $n = 200$, $R = 1$, viscous Burgers' equation, I.C. (6.3).

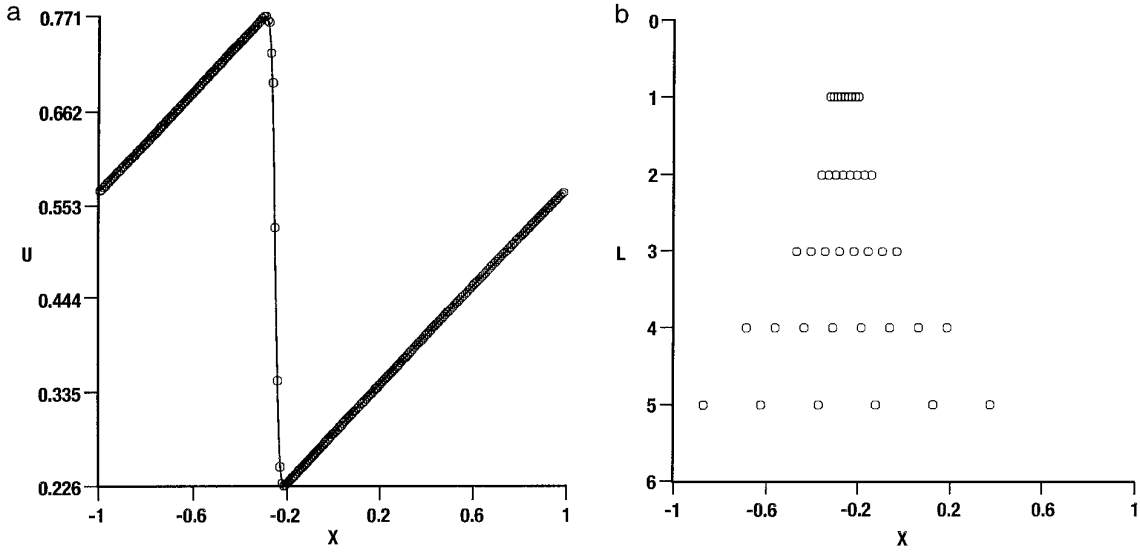

FIG. 10. Solution at $n = 600$, $R = 10$, viscous Burgers' equation, I.C. (6.3).

which is based on (3.7) and assumes an initial discontinuity, is much too pessimistic. Nevertheless, as long as we account for the *worst case* scenario represented by (3.15), multiresolution is safe, although possibly less than optimal. Therefore, we accept (3.15), for the moment, for all problems. As our numerical results will demonstrate, we still get efficiencies of at least around 4 for our model problem.

We now turn to present results for $R = 0.001$, 1, and 10:

(i) $R = 0.001$. The large diffusion keeps the initially smooth data smooth for all time. The efficiency does not change, but eventually we expect it to rise as the extrema further diminish in magnitude. See Table III and Figs. 11a,b for results.

(ii) $R = 1$. At $n = 600$ we have an N-wave (Fig. 12a) and a corresponding multiresolution diagram (Fig. 12b) that resembles that of an inviscid case. The main difference between this and case A(ii) above is the overall higher

TABLE II

Numerical Solution of 1D Viscous Burgers' Equation, I.C. (6.3)

R	n	μ	e_1	e_2	e_∞
0.001	10	2.91	9.28×10^{-6}	3.56×10^{-5}	1.91×10^{-4}
	100	2.64	1.07×10^{-4}	1.88×10^{-4}	7.26×10^{-4}
	200	2.81	2.16×10^{-4}	3.48×10^{-4}	1.20×10^{-3}
	600	3.20	3.79×10^{-4}	4.72×10^{-4}	1.34×10^{-3}
	1000	4.00	6.40×10^{-4}	7.33×10^{-4}	1.76×10^{-3}[a]
1	10	3.05	1.05×10^{-5}	3.52×10^{-5}	3.23×10^{-4}
	100	2.72	1.09×10^{-4}	2.04×10^{-4}	8.41×10^{-4}
	200	2.88	1.60×10^{-4}	2.54×10^{-4}	8.73×10^{-4}[a]
	600	3.16	2.83×10^{-4}	3.79×10^{-4}	1.20×10^{-3}
	1000	3.88	2.98×10^{-4}	3.82×10^{-4}	1.09×10^{-3}
10	10	3.20	2.58×10^{-5}	1.18×10^{-4}	1.23×10^{-3}
	100	3.12	1.93×10^{-4}	4.07×10^{-4}	3.98×10^{-3}
	200	3.71	2.78×10^{-4}	5.55×10^{-5}	4.88×10^{-3}
	600	5.44	2.08×10^{-4}	2.56×10^{-4}	6.42×10^{-4}[a]
	1000	5.95	4.89×10^{-4}	1.62×10^{-3}	1.42×10^{-2}

[a] A figure is enclosed for this particular case.

TABLE III

Numerical Solution of 1D Viscous Burgers' Equation, I.C. (6.4)

R	n	μ	e_1	e_2	e_∞
0.001	10	4.00	9.71×10^{-6}	1.72×10^{-5}	6.02×10^{-5}
	100	4.00	4.19×10^{-5}	5.42×10^{-5}	1.73×10^{-4}
	200	4.00	7.64×10^{-5}	9.15×10^{-5}	2.41×10^{-4}
	600	4.00	2.16×10^{-4}	2.42×10^{-4}	4.54×10^{-4}
	1000	4.00	3.39×10^{-4}	3.78×10^{-4}	6.54×10^{-4}[a]
1	10	4.00	1.46×10^{-5}	2.61×10^{-5}	1.14×10^{-4}
	100	3.66	8.51×10^{-5}	1.37×10^{-4}	4.79×10^{-4}
	200	3.12	1.52×10^{-4}	2.53×10^{-4}	1.25×10^{-3}
	600	4.57	1.47×10^{-4}	1.79×10^{-4}	6.02×10^{-4}[a]
	1000	4.65	1.47×10^{-4}	1.78×10^{-4}	4.48×10^{-4}
10	10	4.00	1.07×10^{-4}	2.29×10^{-4}	8.89×10^{-4}
	100	4.41	1.47×10^{-4}	1.90×10^{-4}	7.71×10^{-4}
	200	5.33	1.48×10^{-4}	1.85×10^{-4}	6.67×10^{-4}[a]
	600	5.57	1.60×10^{-4}	1.97×10^{-4}	6.02×10^{-4}
	1000	5.57	1.47×10^{-4}	1.84×10^{-4}	6.97×10^{-4}

[a] A figure is enclosed for this particular case.

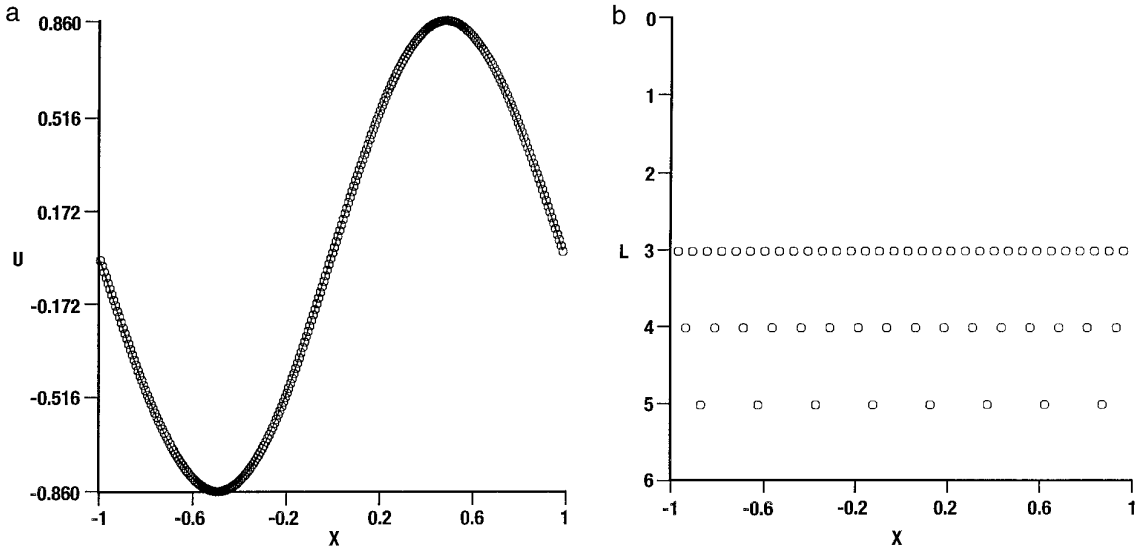

FIG. 11. Solution at $n = 1000$, $R = 0.001$, viscous Burgers' equation, I.C. (6.4).

efficiencies, despite the fact that the same estimate (3.15) is used in both cases for shock width change.

(iii) $R = 10$. Again, for this R, the multiresolution region does not need to be enlarged, and, because of the strong shock sharpening mechanism, we expect high efficiencies. Figure 13a shows the shock that has now become stationary and very sharp. The efficiency is high ($\mu = 5.33$ at $n = 200$ already!) and the multiresolution diagram is correspondingly sparse (Fig. 13b).

With respect to all the numerical runs, we would again emphasize that the errors are quite small in every case, and thus the quality of the solution is not compromised by adding the multiresolution optimization. Overall the results are promising, and they seem to support the previous analysis. The analysis serves to give us a rough estimate in order to modify the multiresolution algorithm previously used for purely hyperbolic problems. This estimate may be further refined, partly by making additional assumptions, or by relying more on numerical experiments. On the other hand, our estimates also show that for high enough Reynolds numbers the viscous problem does not need any special treatment, and the multiresolution scheme developed for hyperbolic conservation laws can be used in its original form.

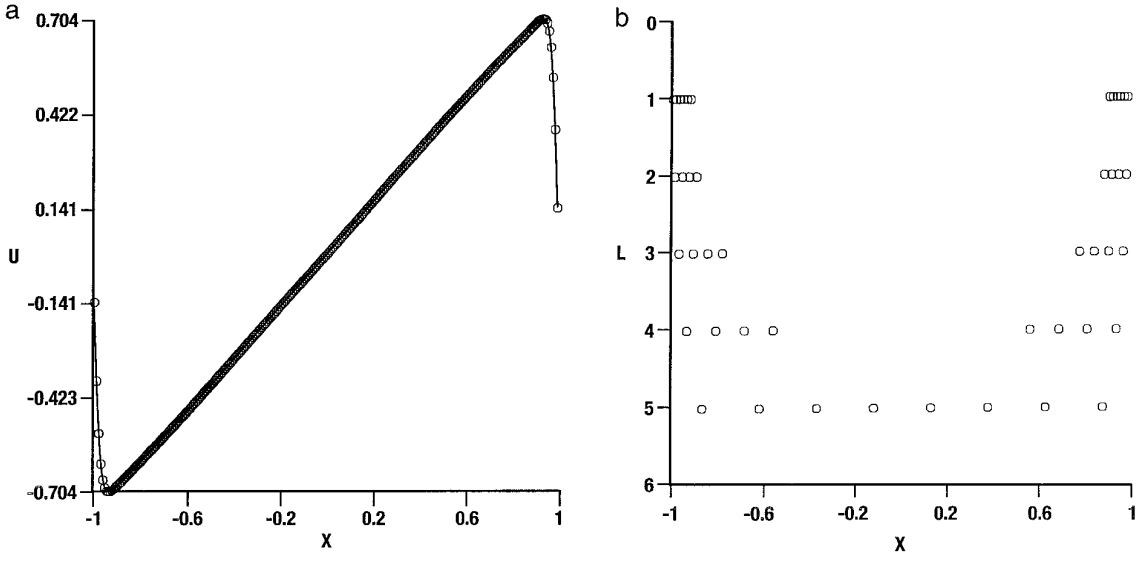

FIG. 12. Solution at $n = 600$, $R = 1$, viscous Burgers' equation, I.C. (6.4).

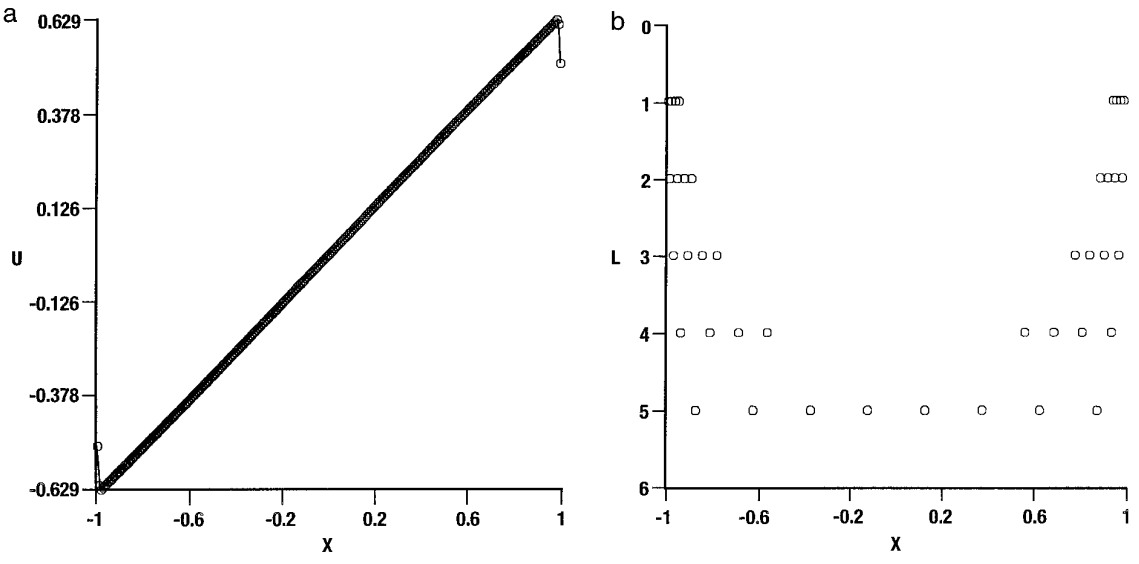

FIG. 13. Solution at $n = 200$, $R = 10$, viscous Burgers' equation, I.C. (6.4).

7. SUMMARY

We presented a modified 1D multiresolution scheme originally developed for hyperbolic conservation laws. Theoretical results for the shock width were given, and subsequently used, together with stability bounds, to provide a reliable estimate for the change in the irregularities' location. The analysis also showed that for low enough viscosity coefficients, no modification of the scheme is needed. Our numerical results in the viscous case are encouraging; for most cases, the efficiency was comparable to the corresponding inviscid problem, indicating the feasibility of multiresolution schemes for the viscous problem also.

The present work can perhaps be considered a first step towards developing multiresolution schemes for full Navier–Stokes equations, where the idea of using shock width estimates should also work. Stability bounds too have been derived for Navier–Stokes equations, and, in conjunction with the shock width, can be used to predict the viscous multiresolution stencil. For systems, as well as for higher order ENO, we expect the payoff from multiresolution speedup to be substantial in terms of actual computational time also.

APPENDIX A

In this appendix we show that, given a fixed time step Δt and all the assumptions of Section 3.2, the largest change in shock width, $\Delta\delta(t) = \delta(t + \Delta t) - \delta(t)$, occurs at $t = 0$.

First, by the mean value theorem, we have that (since δ is differentiable for all $t > 0$):

$$\frac{\delta(t + \Delta t) - \delta(t)}{\Delta t} = \delta'(t^*) \tag{A.1}$$

for some $t^* \in [t, t + \Delta t]$. The quantity $\Delta\delta(t)$ can thus be measured by δ'. Our aim is, therefore, to show that δ' itself is largest at $t = 0$. The simplest way to prove this is to show $\delta'' < 0\ \forall t > 0$.

In order to simplify the algebra, we introduce

$$G(t) = \sqrt{\pi \nu t}\, e^{u_0^2 t/4\nu}\left[1 + E\left(\frac{u_0 t}{2\sqrt{\nu t}}\right)\right], \tag{A.2}$$

so that two consecutive differentiations of (3.7) will now yield

$$\delta' = 8\nu^2 \frac{G'}{(u_0 G + 2\nu)^2} \tag{A.3}$$

and

$$\delta'' = 8\nu^2 \frac{G''(u_0 G + 2\nu) - 2u_0 (G')^2}{(u_0 G + 2\nu)^3}. \tag{A.4}$$

After differentiating (A.2) twice we note:

$$G' = \frac{1}{2}\left[G\left(\frac{1}{t} + \frac{u_0^2}{2\nu}\right) + u_0\right], \tag{A.5}$$

$$G'' = \frac{1}{2}\left[G'\left(\frac{1}{t} + \frac{u_0^2}{2\nu}\right) - \frac{1}{t^2} G\right]. \tag{A.6}$$

We now substitute (A.5) and (A.6) into (A.4) and obtain

$$\delta'' = \frac{8\nu^2}{(u_0 G + 2\nu)^3}\left[-\frac{1}{2} G\left(\frac{u_0^2}{2t} + \frac{\nu}{t^2} + \frac{u_0^4}{2\nu}\right) - \frac{u_0}{2t}\left(\frac{G^2}{t} - \nu\right) - \frac{1}{2} u_0^3 - \frac{1}{4} u_0 G^2 \left(\frac{1}{t} + \frac{1}{2} u_0^2\right)^2 \right]. \quad \text{(A.7)}$$

By observation, all terms within the square bracket are negative, except the expression in the second parenthesis, but for which we have from (A.2),

$$\frac{G^2}{t} - \nu > \nu(\pi - 1) > 0 \quad \text{(A.8)}$$

and thus we conclude that

$$\delta'' < 0 \quad \forall t,\ \nu,\ u_0 > 0. \quad \text{(A.9)}$$

Hence, $\delta'(t)$ will reach its maximum value as $t \to 0$, and so will $\Delta\delta(t)$. This leads to (3.15), and the proof is completed. ▮

APPENDIX B

We show that the approximate region of stability (4.10) implies the von Neumann stability region as required by (4.8); i.e., it is a *sufficient* stability condition.

If we let $\lambda\Delta t = a + ib$, then requirement (4.8), with the definition of κ given by (4.9), is equivalent to

$$(a^2 + b^2 + 2a)^2 + 4(a^2 + 2a) \le 0. \quad \text{(B.1)}$$

Via the substitution

$$A = a^2 + 2a, \quad \text{(B.2a)}$$

$$B = b^2, \quad \text{(B.2b)}$$

(B.1) simplifies to

$$(A + B)^2 + 4A \le 0. \quad \text{(B.3)}$$

On the other hand, the approximate condition (4.10), under the substitutions (B.2), becomes

$$3A + B \le 0. \quad \text{(B.4)}$$

We want to show that (B.4) implies (B.3).

First note that from (B.2a) and (B.1), A satisfies

$$0 \ge A \ge -1. \quad \text{(B.6)}$$

We can therefore write

$$-A \ge A^2 \Leftrightarrow 2\sqrt{-A} - A \ge -3A.$$

The latter of these inequalities, combined with (B.4), now gives (B.3). ▮

ACKNOWLEDGMENTS

The author thanks Stanley Osher for his valuable suggestions related to the nonlinear stability analysis and the use of the travelling wave solution. Also, many thanks to the reviewers for their useful comments.

REFERENCES

1. B. L. Bihari and A. Harten, "Application of Generalized Wavelets: An Adaptive Multiresolution Scheme," in *International Conference on Wavelets, Taormina, Italy, October 1993; J. Comput. Appl. Math.*, **61,** 275–321 (1995).
2. B. L. Bihari and A. Harten, *SIAM J. Sci. Comput.*, to appear.
3. J. D. Cole, *Quart. Appl. Math.* **9,** 225 (1951).
4. C. W. Gear, *Numerical Initial Value Problems in Ordinary Differential Equations* (Prentice-Hall, Englewood Cliffs, NJ, 1971).
5. A. Harten, *J. Comput. Phys.* **115,** 319 (1994).
6. A. Harten, *J. Appl. Numer. Math.* **12,** 153 (1993); UCLA CAM Report 92-08, February 1992.
7. A. Harten, *Commun. Pure Appl. Math.*, to appear; UCLA CAM Report 93-03, March 1993.
8. A. Harten, *SIAM J. Numer. Anal.* **21,** 1 (1984).
9. A. Harten, B. Engquist, S. Osher, and S. R. Chakravarthy, *J. Comput. Phys.* **71,** 231 (1987).
10. C. Hirsch, *Numerical Computation of Internal and External Flows,* Vol. 1 (Wiley, New York, 1989).
11. E. Hopf, *Commun. Pure Appl. Math.* **3,** 201 (1950).
12. K. W. Morton, *Int. J. Numer. Methods Eng.* **15,** 677 (1980).
13. C.-W. Shu and S. Osher, *J. Comput. Phys.* **77,** 439 (1988).
14. J. L. Siemieniuch and I. Gladwell, *Int. J. Numer. Methods Eng.* **12,** 899 (1978).
15. J. Smoller, *Shock Waves and Reaction-Diffusion Equations* (Springer-Verlag, New York/Berlin, 1983).
16. R. S. Varga, *Matrix Iterative Analysis* (Prentice–Hall, Englewood Cliffs, New Jersey, 1965).
17. G. B. Whitham, *Linear and Nonlinear Waves* (Wiley, New York, 1974).